On the applicability of discrete dipole approximation for plasmonic particles

Olli S. Vartia[a], Pasi Ylä-Oijala[b], Johannes Markkanen[c], Salla Puupponen[a], Ari Seppälä[a,*], Ari Sihvola[b], Tapio Ala-Nissila[d,e]

[a] *Department of Energy Technology, Aalto University School of Engineering, P.O. Box 14400, FI-00076 Aalto, Espoo, Finland*
[b] *Department of Radio Science and Engineering, School of Electrical Engineering, Aalto University, P.O. Box 13000, FI-00076 Aalto, Espoo, Finland*
[c] *Department of Physics, University of Helsinki, Helsinki, 00014, Finland*
[d] *Department of Applied Physics and COMP CoE, Aalto University School of Science, P.O. Box 11000, 00076 Aalto, Espoo, Finland*
[e] *Department of Physics, Brown University, Providence, Rhode Island 02912-1843, USA*

Abstract

It has been recognized that the commonly used discrete dipole approximation (DDA) for calculating the optical properties of plasmonic materials may exhibit slow convergence for a certain region of the complex refractive index. In this work we investigate the quantitative accuracy of DDA for particles of different shapes, with silver as the plasmonic material. As expected, the accuracy and convergence of the method as a function of the number of dipoles is relatively good for solid spheres and rounded cubes whose size is of the same order as the wavelength of the localized surface plasmon resonance in silver. However, we find that for solid particles much smaller than the resonance wavelength, and for silver-silica core-shell particles in particular, DDA does not converge to the correct limit even for 10^6 dipoles. We also find that the slow convergence tends to be accompanied by strong, discretization dependent oscillations in the particle's internal electric field. We demonstrate that the main factor behind the slow convergence of the DDA is due to inaccuracies in the plasmonic resonances of the dipoles at the surface of the particles.

Keywords: plasmonic nanoparticles, Discrete dipole approximation, Boundary element method

1. Introduction

The absorption and scattering properties of gold and silver nanoparticles, as seen for example in the colours of stained glass windows, have intrigued

*Corresponding author at: Department of Energy Technology, Aalto University School of Engineering, P.O. Box 14400, FI-00076 Aalto, Espoo, Finland. Tel.: +358 5044 121 10
Email address: ari.seppala@aalto.fi (Ari Seppälä)

people for centuries. In one of the early attempts to understand them, Michael Faraday [1] already noted and studied their unusual appearance. However, it was only over a century ago that the strong absorption and scattering peaks of the spherical metallic nanoparticles were properly explained by Gustav Mie [2]. The peaks are now understood to be caused by localized surface plasmon resonances (LSPR). While Mie theory continues to provide a powerful method for scattering and absorption calculations, its usefulness is limited to highly symmetric particles, such as spheres and ellipsoids. As can be seen from, for example references [3, 4, 5], with modern nanotechnology a wide variety of nanoparticle shapes can be produced.

A number of different numerical methods can be used to calculate the scattering and absorption of arbitrarily shaped nanoparticles. These include the finite-difference time-domain method (FDTD) [6], the boundary element method (BEM) [7] and the discrete dipole approximation (DDA) [8], occasionally also known as the coupled-dipole approximation (CDA). DDA and BEM are based on the volume differential equation (VIE) and the surface integral equation (SIE), respectively. Another difference between them is that DDA is restricted to regular rectilinear grids in its discretization, whereas BEM can use a more accommodating unstructured triangular grid. FDTD on the other hand, differs from BEM and DDA in that instead of solving integral equations, it is based on a direct approach to Maxwells equations. Because FDTD works in the time domain, it has the benefit of being able to analyze a large portion of the spectrum simultaneously.

DDA has been shown to be a relatively simple to use and in some cases extremely accurate [9] method, whose convergence has been analytically studied by Yurkin et al. [10] and according to Mishchenko et al. [11] is numerically exact. A comprehensive overview of the method and of its recent developments has been given by Yurkin and Hoekstra [12]. DDA has naturally been used in many different areas, including the study of plasmonic nanoparticles [13, 14, 15, 16, 17].

Certain unusual behavior of DDA regarding the plasmonic particles has been reported, however. Hao et al. [13] found that the electric field near the surface of the silver particles modelled converges very slowly with dipole count. Yurkin et al. [18] found that in the near-IR wavelengths, 100 nm gold spheres had an error of $10-20\%$ in absorption, even for extremely fine discretizations. Further on Yurkin has comprehensively analyzed DDA's convergence [19] and published a map of it [20] including the region of the complex refractive index which is pertinent to the study of plasmonic nanoparticles. This map shows that the convergence of DDA is much slower near and in the region of the refractive index of silver for optical wavelengths. Karamehmedović et al. [21] discovered that DDA produces an unphysically varying internal electric field for silver particles, while Kelly et al. [14] presented a similar looking polarization distribution in trigonal silver prisms.

In the following sections we briefly describe the methods that are used here and investigate DDA's behavior in the region where the DDA experiences the aforementioned problems. The results are compared to BEM and Mie theory

and special attention is paid to the accuracy of the internal electric fields of the particles. The cause for the problems has been suggested to be shape error on the surfaces [18, 19], and this especially seems to affect plasmonic particles.

2. Methods

2.1. Discrete dipole approximation

The discrete dipole approximation (DDA) is a general method for simulating scattering and absorption of electromagnetic waves for arbitrarily shaped particles. Since it was originally developed by Purcell and Pennypacker [8] DDA has been implemented and generalized in different ways, ADDA [22] and DDSCAT [23] being the two major freely available implementations.

DDA is based on the volume integral equation (VIE), in which the electric field $\bar{E} = \bar{E}^{inc} + \bar{E}^{sca}$, which consists of the field of the incident plane wave $\bar{E}^{inc}$ and the scattered field $\bar{E}^{sca}$, can be written as [24]

$$\begin{aligned}\bar{E}(\bar{r}) =& \bar{E}^{inc}(\bar{r}) + \lim_{\delta V \to 0} k_0^2 \int_{V-\delta V} \mathrm{d}\bar{r}' \left(\epsilon_r(\bar{r}') - 1\right) \bar{\bar{G}}(\bar{r}, \bar{r}') \cdot \bar{E}(\bar{r}') \\ & - \left(\epsilon_r(\bar{r}) - 1\right) \bar{\bar{L}} \cdot \bar{E}(\bar{r}) \quad .\end{aligned} \tag{1}$$

Here k_0 is the wave number in vacuum and $\epsilon_r(\bar{r})$ is the complex relative permittivity. The scattered field is written as a volume integral over the volume of the particle V, from which an infinitesimal volume δV around $\bar{r}$ has been excluded. This is done in order to avoid a singularity, and the excluded volume is taken into account by using the source dyadic $\bar{\bar{L}}$. The source dyadic depends on the shape of the excluded volume and is usually chosen to be $\bar{\bar{L}} = \frac{1}{3}\bar{\bar{I}}$, which corresponds to a spherical volume. $\bar{\bar{I}}$ is the unit dyadic. $\bar{\bar{G}}(\bar{r}, \bar{r}')$ is the dyadic Green's function of free space, which can be written in matrix form as

$$\bar{\bar{G}}(\bar{r}, \bar{r}') = \begin{pmatrix} k_0^2 + \frac{\partial^2}{\partial x'^2} & \frac{\partial^2}{\partial x' \partial y'} & \frac{\partial^2}{\partial x' \partial z'} \\ \frac{\partial^2}{\partial y' \partial x'} & k_0^2 + \frac{\partial^2}{\partial y'^2} & \frac{\partial^2}{\partial y' \partial z'} \\ \frac{\partial^2}{\partial z' \partial x'} & \frac{\partial^2}{\partial z' \partial y'} & k_0^2 + \frac{\partial^2}{\partial z'^2} \end{pmatrix} \frac{1}{k_0^2} g(\bar{r}, \bar{r}'), \tag{2}$$

where

$$g(\bar{r}, \bar{r}') = \frac{e^{ik_0|\bar{r} - \bar{r}'|}}{4\pi|\bar{r} - \bar{r}'|} \quad , \tag{3}$$

is the scalar free space Green's function.

After discretization into N dipoles we arrive at the form

$$\bar{\bar{\alpha}}_i^{-1} \bar{p}_i - \frac{k_0^2}{\epsilon_0} \sum_{i \neq j}^{N} \bar{\bar{G}}_{ij} \cdot \bar{p}_j = \bar{E}_i^{inc} \quad , \tag{4}$$

where $\bar{\bar{\alpha}}_i$ is the polarizability tensor, which gives the relationship between the dipole moment $\bar{p}_i$ of an element and the electric field as $\bar{p}_i = \bar{\bar{\alpha}}_i \cdot \bar{E}_i$. There

is some freedom in the choice of the polarizability and many different kinds of polarizabilities have been implemented [25, 26, 27, 28, 29, 30, 31], with radiative corrections to account for the finite size of the volume element, etc. However, most of the implementations reduce to DDA with the Clausius–Mossotti polarizability

$$\alpha_i^{CM} = 3\epsilon_0 \frac{\epsilon_r - 1}{\epsilon_r + 2} V_i \quad , \tag{5}$$

in the long wavelength limit [32], provided that the lattice of dipoles is cubic. An example of this can be seen in Fig. 11. There are a couple of implementations that may act differently at the long wavelength limit, namely the filtered coupled dipole formulation (FCD) [31] and the integrated Green's tensor (IGT) formulation [27].

DDA can be used to calculate many different kinds of data, Mueller matrix elements, radiation torque, etc. The data discussed in the later sections consists of absorption and scattering efficiencies Q_{abs} and Q_{sca} and electric field strengths E in the near field regime. The different efficiencies Q_i are defined as $Q_i = C_i/\pi a_{\text{eff}}^2$, where a_{eff} is the radius of a sphere that has the same volume as the particle considered and C_i is the absorption or scattering cross section of the particle, depending on which efficiency is in question.

Although it is commonly known that very high complex refractive indices $\tilde{n} = n + ik$ may cause DDA to converge slowly, problems can also appear when the absolute value of the complex refractive index is small, if $\tilde{n}$ is mostly imaginary [13, 18, 19, 20]. In this region unphysically varying internal electric fields have also been reported [21].

It is worth noting that for non-magnetic materials the complex index of refraction $\tilde{n}$ holds the same information as the complex permittivity ϵ_r and the two are related by $\epsilon' = n^2 + k^2$ and $\epsilon'' = 2nk$. The conditions for achieving accurate results with DDA when using particles much smaller than the wavelength λ_0 are not as clear cut as for larger particles. The only clear rule for nanoparticles is that the discretization must be fine enough to present the shape of the particle in sufficient detail, however a much finer discretization may in some cases be necessary and this must unfortunately be determined on case by case basis.

2.2. Boundary element method

For modeling solid and layered core-shell particles the surface integral equation method (SIE) starts by dividing the structure into homogeneous regions, i.e., regions with a constant refractive index. Then, with the surface equivalence principle and application of the electromagnetic interface conditions - continuity of the tangential components of the electric field $\bar{E}$ and the magnetic field $\bar{H}$ - the original problem of solving Maxwell's equations in the entire three dimensional space is reformulated as an equivalent problem of solving current sources from surface integral equations [7]. The resulting surface integral equations are discretized using the boundary element method (BEM) with Galerkin's

testing procedure and Rao–Wilton–Glisson (RWG) functions. In this process, the equivalent surface current densities on the surfaces, electric $\bar{J}$ and magnetic $\bar{M}$, are first approximated with a linear combination of the RWG basis functions [33]. Then in Galerkin's method, the equations are multiplied with testing functions that are identical with the basis functions via a symmetric L^2 product. Special integration routines are necessary to evaluate the associated singular integrals with sufficient accuracy [34, 35], in particular, in the case of strongly resonating particles and in the near field regions. By solving the matrix equation, the coefficients of the RWG approximations of the equivalent current densities on the interfaces of the regions can be determined. With these coefficients both the near and far fields can be evaluated outside the surfaces. The scattering and absorption efficiencies can be obtained with the BEM matrices as shown in [36].

3. Results

3.1. Parameters and geometry

Scattering and absorption efficiencies were calculated for different particles and densities of discretization, with special attention paid to the positions of the plasmonic absorption and scattering peaks. The particles that were studied were two $D = 10$ and 100 nm diameter silver spheres, a round cornered cube with a $a = 50$ nm side length and two 50 nm diameter spherical silica-silver core-shell particles with diameter ratios of 0.6 and 0.9. Three numbers of dipoles were used for each particle, 10^5, 5×10^5 and 10^6. Even larger numbers of dipoles are possible, especially by using ADDA, however a limit had to be drawn somewhere in order to keep resources used at a reasonable level. The discretizations can be seen in Table 1.

The material properties of silver are calculated using the Drude model

$$\epsilon_{Ag}(\lambda_0) = \epsilon_\infty - \left(\frac{\lambda_0}{\lambda_p}\right)^2 \frac{1}{1 + i\frac{\lambda_0}{\lambda_d}} \quad , \tag{6}$$

with values $\epsilon_\infty = 5.5$, $\lambda_p = 130$ nm and $\lambda_d = 30\,\mu$m, which were calculated from data by Johnson and Christy [37] by Wallén et al. [38]. All of the DDA data that are presented in the figures were calculated using DDSCAT 7.3 with the Gutkowicz-Krusin & Draine polarizability (GKDLDR), and ADDA was used to confirm that the results were not dependent on the code, but a property of the method.

The two sizes of silver spheres were chosen because they behave differently in the plasmonic region, as for the small $D = 10$ nm sphere absorption dominates, whereas for the $D = 100$ nm sphere scattering is more important.

The shape of the round cornered cube was constructed by using a superquadric equation

$$|x|^p + |y|^p + |z|^p = \left(\frac{a}{2}\right)^p \quad , \tag{7}$$

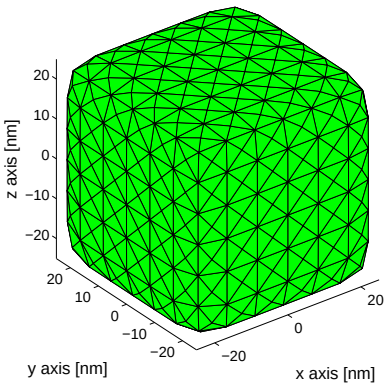

Figure 1: A mesh similar to the one used in BEM for the rounded cube calculations. This particular mesh has 864 elements. The exponent from Eq. (7) is $p = 10$.

Table 1: The lattice spacings for the shapes and discretizations that were used.

Shape	10^5 dipoles	$5 \cdot 10^5$ dipoles	10^6 dipoles
10 nm sphere	0.175 nm	0.102 nm	0.081 nm
100 nm sphere	1.753 nm	1.021 nm	0.813 nm
rounded cube	1.085 nm	0.624 nm	0.49 nm
both core-shell particles	0.876 nm	0.51 nm	0.406 nm

with $p = 10$ as the exponent and $a = 50\,\text{nm}$. It should be noted that the rounded cube is different from the other particles because it does not have spherical symmetry. The DDA computations were only performed for the orientation where $\bar{k}_0 || \hat{x}$ and $\bar{E}^{inc} || \hat{y}$, i.e., no orientational averaging was used. An example of what a rounded cube model produced using Eq. (7) looks like can be seen in Fig. 1

Two core-shell particles were also considered in order to test DDA with particles that have more complex structure. Both of the core-shell particles consisted of a spherical silica core surrounded by a concentric spherical silver shell. The refractive index of silica was set to constant $n_{\text{SiO}_2} = 1.50$. As mentioned before, two different core-to-shell ratios were used, $D_{core}/D_{shell} = 0.6$ and $D_{core}/D_{shell} = 0.9$. The outer diameters of both particles were 50 nm.

Simulating infinitely long structures is possible using DDSCAT [39] and this was also taken advantage of. Two infinite structures were tested, namely the internal electric fields of a 50 nm thick infinite silver film and a 100 nm diameter infinite cylinder were calculated for the case of an incoming plane wave with $\lambda_0 = 400\,\text{nm}$. For both the cylinder and the film the dipole lattice spacing $d = 1\,\text{nm}$ was used.

The DDA results were compared to BEM, which has been found to have good convergence in all of the regions where comparisons were made.

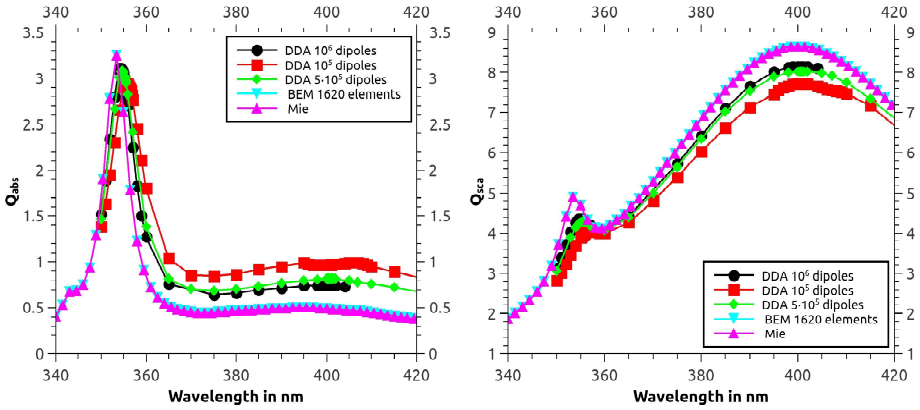

Figure 2: The absorption and scattering efficiencies of a 100 nm diameter silver sphere in vacuum, calculated using DDA, BEM and the analytic Mie solution.

The DDA was also compared to another volume integral based method of moments (MoM) implementation, which is more flexible in the choice of discretization grid. Instead of using dipole approximation with polarization factors, this method solves the volume integral equation using other basis and testing functions.

3.2. Convergence with increasing dipole count

Convergence with increasing dipole count can be seen in Figs. 2-6 for the 100 nm sphere, the 10 nm sphere, the 50 nm round cornered silver cube, and the two core-shell particles with ratios $D_{core}/D_{shell} = 0.6$ and $D_{core}/D_{shell} = 0.9$, respectively. All of these results are compared with BEM and for the spheres and the core-shell particles with the analytic Mie solutions. In general, quite a large number of dipoles seems to be necessary until the results start to converge. For the 100 nm and 10 nm spheres, the location of the resonance peak of the DDA data is quite close to the analytic solution; however, the amplitude of the resonance is lower. The best case scenario for DDA seems to be the 100 nm sphere, while the case of the rounded cube also converges faster than the other particles tested. DDA has great difficulties with the core-shell particles and still cannot correctly find the plasmonic resonance for the case with ratio 0.9 even when using up to 10^6 dipoles.

3.3. Internal fields

The internal electric fields were also calculated for selected particles and wavelengths. Fig. 7 illustrates what happens to the internal field as disctretization is made finer in the case of the absorption peak in the 10 nm silver sphere.

Similarly to Fig. 7, the internal fields of an infinitely long 100 nm diameter silver cylinder and an infinite 50 nm thick silver film were also calculated. The

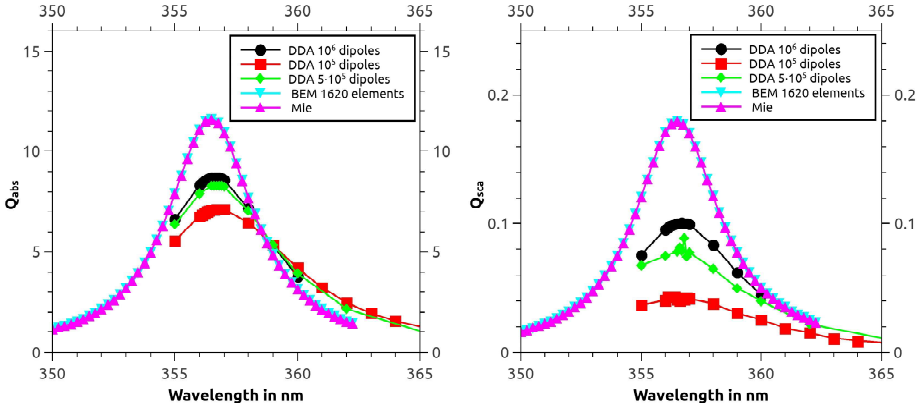

Figure 3: The absorption and scattering efficiencies of a 10 nm diameter silver sphere in vacuum, calculated using DDA, BEM and the analytic Mie solution.

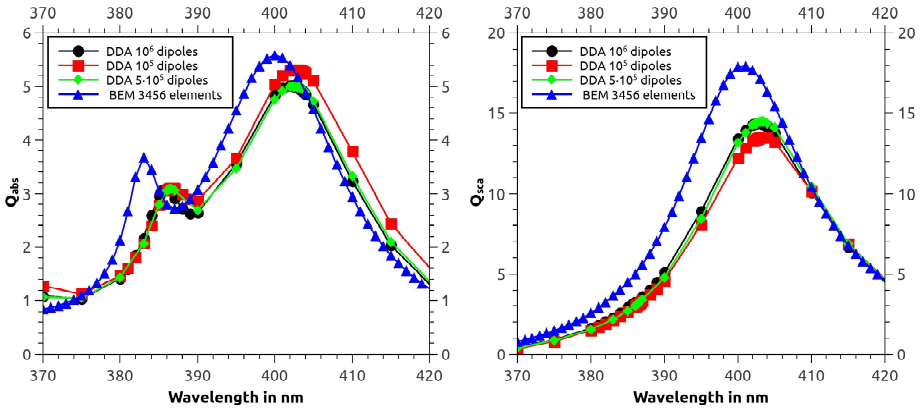

Figure 4: The absorption and scattering efficiencies of a rounded silver cube in vacuum, with a 50 nm side length, calculated using DDA and BEM. The exponent for the shape from Eq. (7) is $p = 10$.

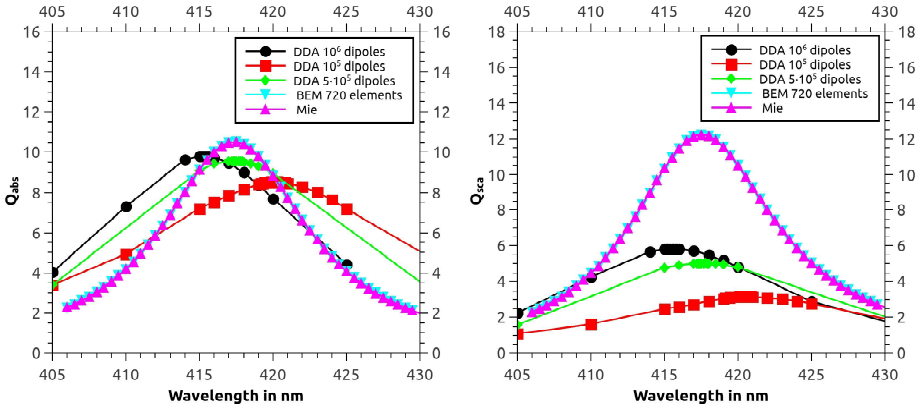

Figure 5: The absorption and scattering efficiencies of a 50 nm $SiO_2 - Ag$ core-shell particle with a core-shell ratio of 0.6, in vacuum, calculated using DDA, BEM and the analytic Mie solution. Note that the layer of dipoles which represents the silver shell in DDA is relatively thin and this compounds with the problems of getting a correct field at the surface of the particle as all of the dipoles that should dictate the particle's behavior are there.

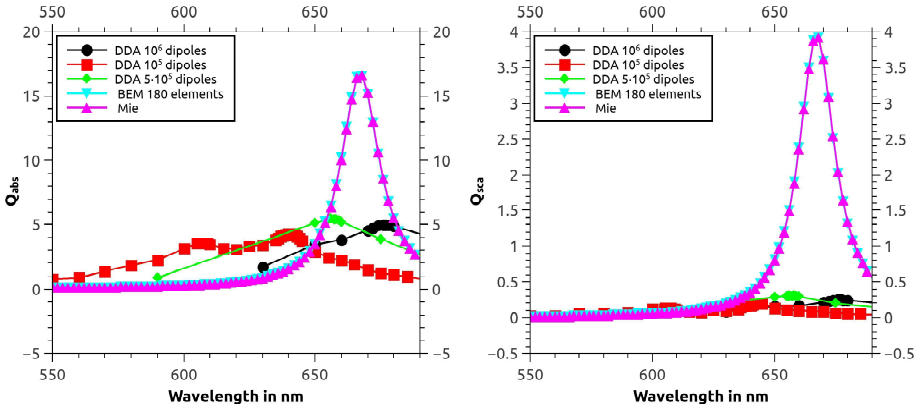

Figure 6: The absorption and scattering efficiencies of a 50 nm $SiO_2 - Ag$ core-shell particle with a core-shell ratio of 0.9, in vacuum, calculated using DDA, BEM and the analytic Mie solution. Note that the layer of dipoles which represents the silver shell in DDA is very thin and this compounds with the problems of getting a correct field at the surface of the particle as all of the dipoles that should dictate the particle's behavior are there.

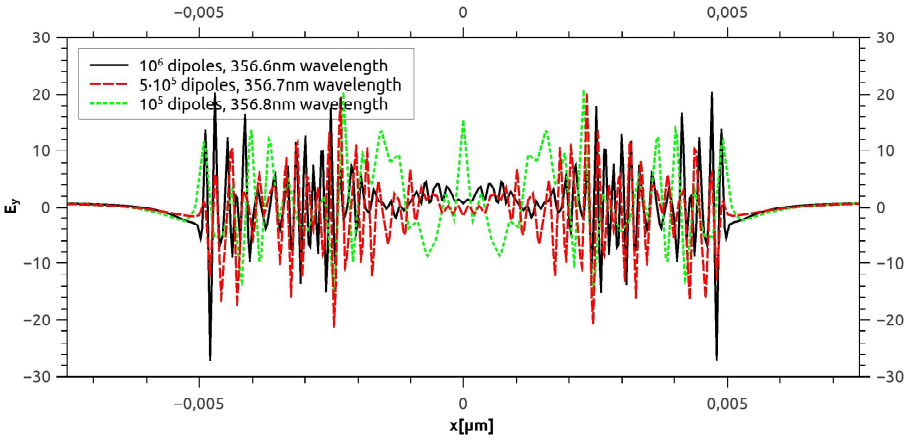

Figure 7: The strength of the electric field along the x-axis of a 10 nm Ag sphere, through its center, at the absorption peak. The incident electric field is polarized along the y-axis and the wave travels along the direction of the x-axis, i.e., $\bar{k}_0||\hat{x}$ and $\bar{E}_0||\hat{y}$. The boundaries of the sphere are at $x = -0.005\,\mu$m and $x = 0.005\,\mu$m. Note that while the internal fields vary strongly for the different discretizations, the external fields stay fairly similar.

variation of the electric field along a line that goes through the cylinder perpendicularly to its axis can be seen in Fig. 8 for the cases where the cylinder is parallel and perpendicular to the incoming field, respectively. The variation of the electric field along a line that goes through the 50 nm thick silver film can be seen in Fig. 9.

3.4. Dependence of accuracy on the complex refractive index

In order to study the region of anomalously low performance of DDA further, a sphere with diameter $D = 0.1\,\mu$m was tested at $\lambda = 400$ nm using several different complex refractive indices $\tilde{n}$. Specifically, the internal electric field within the sphere along its x-axis ($\bar{k}_0||\hat{x}$) was calculated, because it was found that the accuracy problems characteristic of plasmonic particles were always accompanied by a strongly varying internal electric field. The fields were then compared with results produced by the SIE based BEM, for which the same problems do not appear. The results of these these calculations can be seen in Fig. 10. For DDA 10^5 dipoles were used in these calculations.

One might think that the unphysical internal electric field in Fig. 10 arises from the vicinity of the plasmonic resonance; however, it was found that the same variation in the electric field arises also when the absolute value of the refractive index is kept at $|\tilde{n}| = 1.5$. Other values of material properties were also tested from $|\tilde{n}| = 0.71$ to $|\tilde{n}| = 2.24$ or in terms of ϵ_r, $|\epsilon_r| = 0.5$ and $|\epsilon_r| = 5$. They all showed the same result; always when the real part of $\tilde{n}$ approaches zero the internal electric field of the particle starts to oscillate strongly. An important feature is also that both ADDA and DDSCAT produced similar results. Several

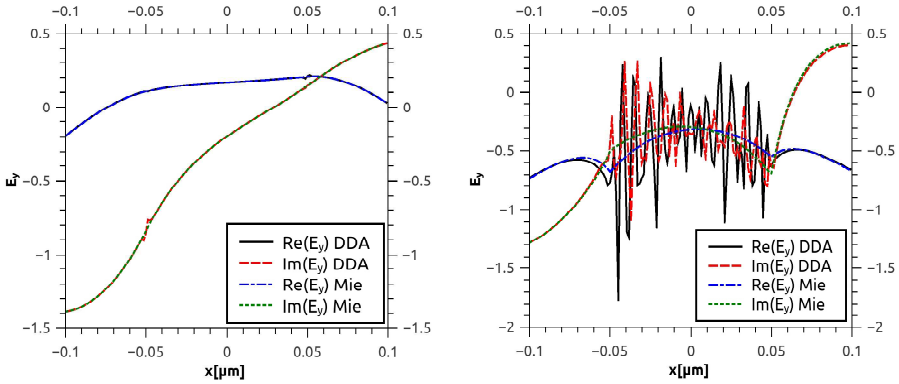

Figure 8: The electric field inside an infinite silver cylinder. The incoming wavelength is $\lambda_0 = 400\,\text{nm}$ and the boundaries of the cylinder are at $x = -0.05\,\mu\text{m}$ and $x = 0.05\,\mu\text{m}$. DDA data are compared with the analytical Mie solution. *Left:* The cylinder is parallel to the incident electric field, but perpendicular to the wave vector. This means that $\bar{E}$ is continuous on the surface of the cylinder. The computational data agree with the analytic solution. *Right:* The cylinder is perpendicular to both the incident electric field and the wave vector. The component of $\bar{E}$ which is perpendicular to the surface has a discontinuity, which leads to an excess charge density on the surface. The computational result clearly fails to capture the correct behavior of the internal field.

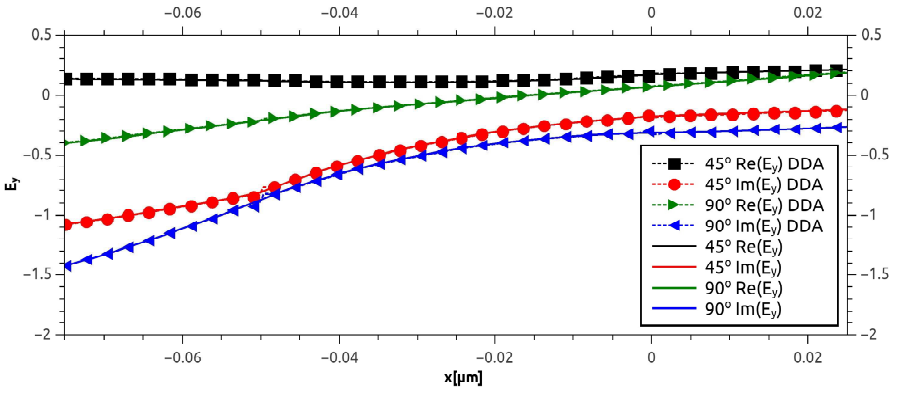

Figure 9: The electric field inside an infinite silver film, which is 50 nm thick. The incoming wavelength is $\lambda_0 = 400\,\text{nm}$. In the data marked $45\,^\circ$, the wave vector forms a $45\,^\circ$ angle with the film, which is in the yz-plane. The polarization of the incoming wave is parallel to the scattering plane, which is here the xy-plane. In the data marked $90\,^\circ$, the incoming wave vector is perpendicular to the surface of the film. E_y is the y-component of the electric field. Both DDA data and the analytical solutions are presented. DDA data seems to agree with the analytical solution. The film starts at $x = -0.05\,\mu\text{m}$ and ends at $x = 0.0\,\mu\text{m}$.

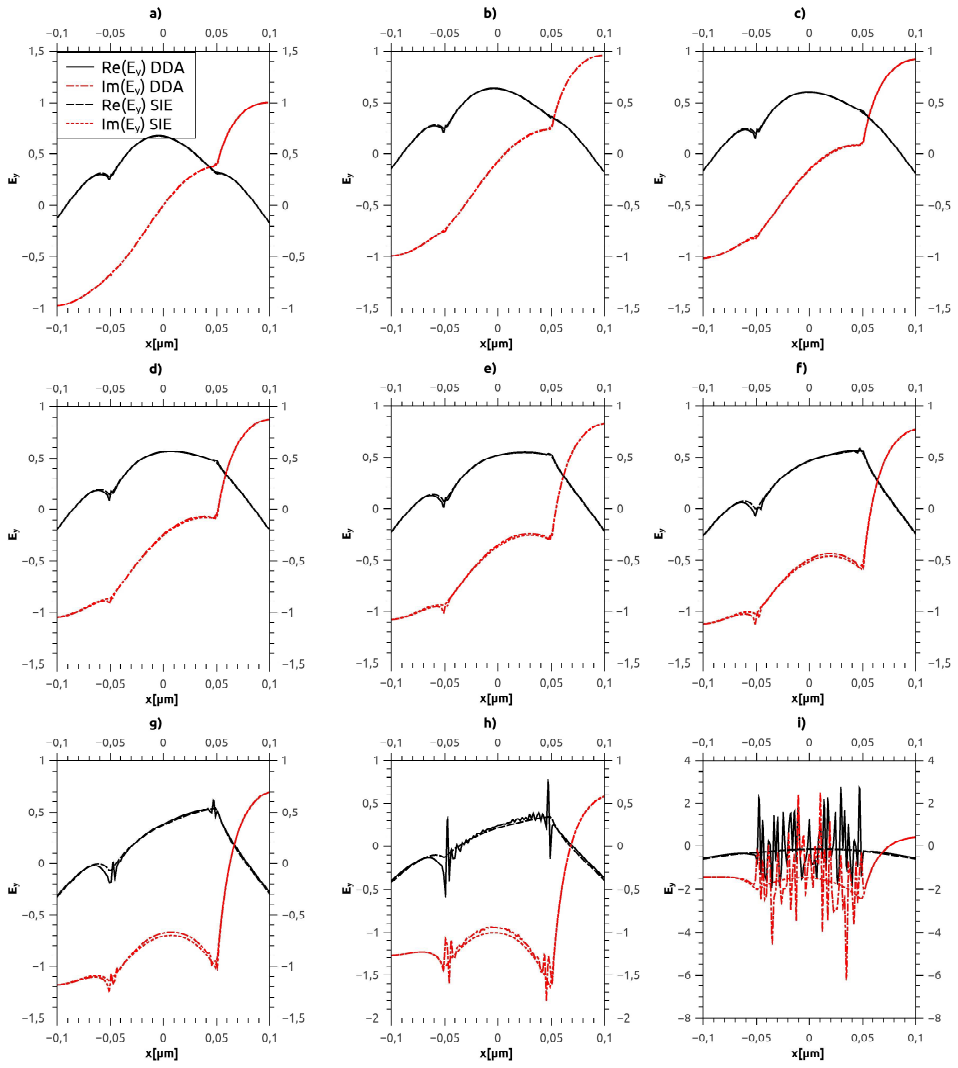

Figure 10: The internal electric field E_y for different values of $\tilde{n}$ along a circle arc in the complex plane, while keeping $|\tilde{n}| \approx 2$. The argument of $\tilde{n}$ goes from $\varphi = \pi/10$ to $\varphi = 1.5545521 \approx \pi/2$, throughout a) to i) with steps of $\Delta\varphi = \pi/20$. The last step i) is the complex refractive index of silver. The boundaries of the sphere are at $x = -0.05\,\mu$m and $x = 0.05\,\mu$m.

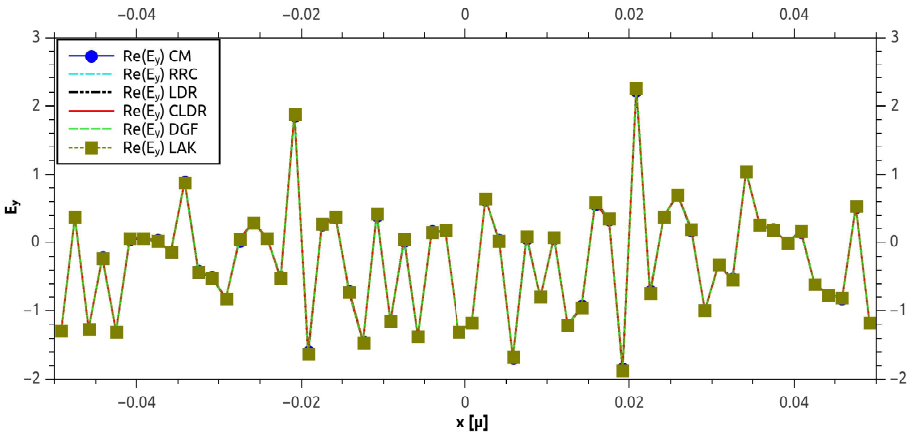

Figure 11: The internal electric field of a 100 nm diameter silver sphere calculated using different polarizabilities implemented in ADDA. Wavelength is 400 nm, refractive index is $\tilde{n} = 0.032496 + 2.000264i$ and the lattice spacing is 1.667 nm. The different polarizabilities used in the figure are the corrected lattice dispersion relation (CLDR) [25], the digitized Green's function (DGF) [26], the radiative reaction correction (RRC) [28], the default lattice dispersion relation (LDR) [29], the Clausius–Mossotti polarizability (CM) and Lakhtakia's formulation (LAK) [30].

different polarizabilities and numerical methods were also tested, and because of the fineness of the discretization, they all produced almost identical electric fields. This means that although the field looks random, it is in fact specific to the discretization. An example of the influence of different polarizabilities can be seen in Fig. 11. It should be noted, however, that using the FCD- or IGT-interaction instead of the more traditional point-interaction, may lead to different results in the long wavelength limit.

3.5. Effect of the cubic discretization grid

We also attempted to compute the optical properties of a spherical silver particle $D = 100\,\text{nm}$ at $\lambda = 400\,\text{nm}$ using another volume-integral-equation (VIE) based method of moments, which allows the use of different kinds of discretizations. We apply so-called JVIE-formulation [40] employing piecewise constant basis and testing functions associated with tetrahedral or cubic elements. The sphere was discretized with 4357 tetrahedral elements or $64 \times 64 \times 64$ cubic grid.

Here it was found that the problems depend on the choice of the computational grid. As can be seen in Fig. 12, a cubic grid produced the same problematic results as DDA, whereas the results produced by a tetrahedral grid were accurate and convergence was achieved in a reasonable time and with far fewer elements. It should be noted that in contrast to the DDA, the applied JVIE-formulation attempts to enforce the interface conditions to be valid in a

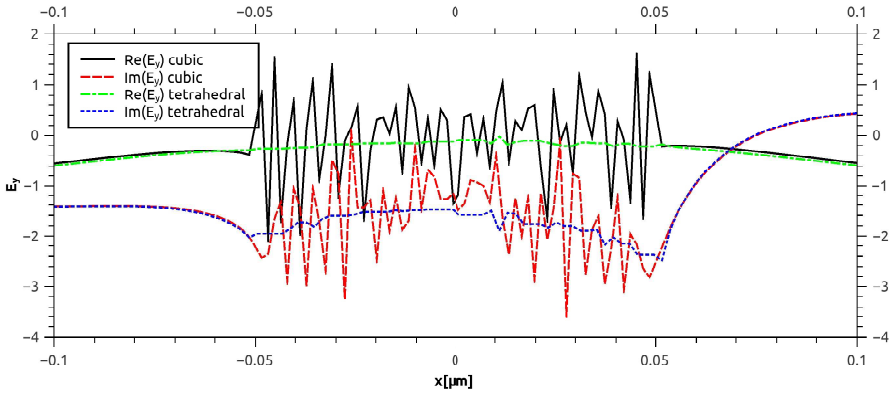

Figure 12: The y-component of the electric field along the x-axis of a 10 nm silver sphere, through its center, at 400 nm wavelength. The curves were calculated using a VIE based method of moments with two different kinds of discretizations, cubical and tetrahedral. The incident electric field is polarized along the y-axis and the wave travels along the direction of the x-axis, i.e., $\bar{k}_0 || \hat{x}$ and $\bar{E}_0 || \hat{y}$. The boundaries of the sphere are at $x = -0.05\,\mu$m and $x = 0.05\,\mu$m.

weak sense. Hence, the method tries to model surfaces exactly as they are discretized. Despite this fundamental difference between the DDA and the JVIE with cubic cells, it is interesting that both methods show similar breakdown in the case of plasmonic nanoparticles. It should be noted, however, that piecewise constant basis functions for cubic elements may not span an appropriate basis since they do not have enough degrees of freedom to model surface charges. This, in turn, may give rise to spurious charges which may be detrimental to the stability and the solution accuracy.

More specifically, the Helmholtz decomposition states that any L^2 vector function can be represented as

$$\bar{f} = \nabla \times \bar{v} + \nabla u \quad , \tag{8}$$

in which v and u belong to the appropriate function spaces (see, e.g. [41] and references therein). The harmonic part of the Helmholtz decomposition is included in u. The ∇u functions are related to equivalent surfaces charges when piecewise constant basis functions are used. The number of faces in a given mesh is N_f. For a tetrahedral mesh, it can be shown that the dimension of this space is $N_f - 1$ assuming that the object is simply-connected. One linearly dependent face charge is due to the charge neutrality—with the piecewise constant basis it is impossible to represent non-zero total charge. For a cubic mesh, however, the number of degrees of freedom for the ∇u functions is less that $N_f - 1$. This means that surface charges are not associated to the faces of cubes or there are too many dependent surface charges. Detailed analysis is, however, out of the scope of this paper. More discussion on the significance of triangular and

quadrilateral grids and linear basis functions can be found, for example in [42].

4. Discussion

It is clear from Figs. 2-6 that a very large number of dipoles in DDA is needed in order to get results with good accuracy. Even in this case the internal electric field is still unphysical and shows no improvement, as can be seen in Fig. 7. This is in agreement with the region of slow convergence previously found by Yurkin [19, 20], i.e. $\mathrm{Re}[\tilde{n}] \to 0$, or in terms of permittivity $\epsilon_r = \epsilon' + i\epsilon''$, $\epsilon' < 0$ and $\epsilon'' \to 0$. A similar conclusion was previously also made by Andersen et al. [43] for SiO_2 and SiC particles in the infrared region. The problems seem to originate from the surface of the structure. This has been suggested before by Yurkin et al. [18, 19], as well as by Andersen et al. [43] and seems especially clear from Figs. 5 and 6. The cases with the worst problems are indeed the ones with the largest fractions of dipoles on surfaces.

The problems with the plasmonic particles can be understood by examining the difference between the polarizability of the volume elements that are used on the surface in DDA and the polarizabilities of the elements that would have to be used in order to get the shape of the surface modeled correctly. At the long wavelength limit all of the volume elements in DDA have the same Clausius–Mossotti polarizability α_{CM}, which is essentially the polarizability of a dielectric sphere or a cube. Of course, a smooth surface cannot be constructed out of a cubic grid, except for the special case of infinite planar surfaces.

For a curved surface, different points in the cubic grid will have different distances from the ideal surface modeled. If the depth of a dipole from the surface of the model is smaller than the radius of the volume of the material that the dipole is meant to represent, it seems reasonable to treat this volume as a truncated version of the element that is otherwise used. Here it is important to note that for a curved surface and a cubic grid there will be a variety of different truncations, no matter how fine the discretization. In fact, the finer the discretization, the larger the variety of shapes of volume elements at the surface.

The truncated element is no longer symmetric and consequently its polarizability will also be asymmetric. The shape of a volume element is taken into account by the use of the source dyadic $\bar{\bar{L}}$ in Eq. (1). The general form of $\bar{\bar{L}}$ is

$$\bar{\bar{L}} = \frac{1}{4\pi} \int_{\delta S} \frac{\hat{n}\hat{r}'}{r'^2} \mathrm{d}S' \quad , \tag{9}$$

where δS is the surface of the volume element and $\hat{n}$ is the surface normal. As has been shown by Yaghjian [24], as long as the origin stays inside the volume element, the diagonal elements of $\bar{\bar{L}}$ always satisfy

$$L_{xx} + L_{yy} + L_{zz} = 1 \quad . \tag{10}$$

The polarizability tensor of an arbitrarily shaped volume element is

$$\bar{\bar{\alpha}} = \left\{ \frac{1}{\epsilon_0 V(\epsilon_r - 1)} \left[\bar{\bar{I}} + (\epsilon_r - 1)\bar{\bar{L}} \right] \right\}^{-1} \quad , \tag{11}$$

which can be arrived at by discretizing and reorganizing Eq. (1). When $\bar{\bar{L}}$ is diagonal the diagonal elements are called the depolarization factors $L_{ii} = N_i$ and the polarizability tensor $\bar{\bar{\alpha}}$ also becomes diagonal

$$\alpha_i = \epsilon_0 V \frac{\epsilon_r - 1}{1 + N_i(\epsilon_r - 1)} \quad , \tag{12}$$

which reduces to the Clausius–Mossotti polarizability when the $N_i = \frac{1}{3}$, i.e., for a sphere or a cube. Now if we look at Eq. (12), we see that α_i has a singularity and also changes its sign at

$$\epsilon_r = 1 - \frac{1}{N_i} \quad , \tag{13}$$

which turns out to be the same formula that Andersen et al. [43] came up with.

Our view is that the differences between the DDA solution and an analytic solution are not caused by resonant behavior of the individual elements in DDA, but rather by the lack of such behavior. In other words, if the elements on the surface had correct polarizabilities, they would have resonances at different values of ϵ' depending on their shape, instead of just at $\epsilon' = -2$, as is the case in the current implementations of DDA, which use the same polarizability for all of their elements. Under the usual conditions for DDA, i.e., when $\epsilon' > 0$, no resonant behavior can occur and the influence of the finite error in polarizabilities at the surface can be made negligible, because the number of dipoles within the particle vastly outnumber the dipoles on the surface. However, in the region where resonant behavior is possible, i.e., when $\epsilon' < 0$, the error in the surface polarizability can grow very large and so also a very large number of dipoles is needed in order to compensate for the error on the surface.

Surface features made up of multiple dipoles that are due to the cubic grid in DDA may have their own additional resonances, as may be seen in the left panel of Fig. 14. These should not appear if the shapes of the volume elements on the surface are properly taken into account.

Now, if we actually solve Eq. (9) for the case of a sphere intersected by a plane normal to the z-axis, we get

$$L_{zz} = \frac{1}{2}\left(\cos\theta_0 - \frac{\cos\theta_0}{|\cos\theta_0|} \right) + \frac{1}{6}\left(1 - \cos^3\theta_0\right) \quad , \tag{14}$$

$$L_{xx} = L_{yy} = \frac{1}{48}\left[\cos(3\theta_0) - 9\cos\theta_0 + 8\right] \quad . \tag{15}$$

Here the angle θ_0 gives us the intersection of the plane and the sphere, $\theta_0 = \pi/2$ corresponds to a hemisphere and $\theta_0 = \pi$ corresponds to a complete sphere. It is

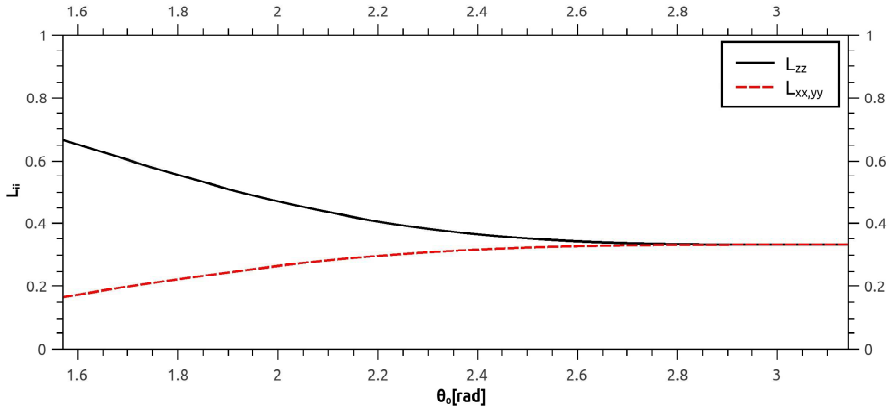

Figure 13: The components of the self dyadic $\bar{\bar{L}}$ for a sphere intersected by a plane normal to the z-axis. The angle θ_0 is the angle between the intersection and the z-axis, the center of the sphere being in the origin. Only the cases where the origin is inside the shape are considered, i.e. $\pi/2 < \theta_0 \leq \pi$.

reasonable to only consider the cases where the center of the element is inside the volume, as the whole point of having an exclusion volume is to contain that center. The values the L_{ii} go through can be seen in Fig. 13 L_{zz} varies between 1/3 and 2/3, while the L_{xx} and L_{yy} vary between 1/6 and 1/3. Looking at Eq. (13) we see that these correspond with resonances at $-2 < \epsilon_r \leq -1/2$ and $-6 < \epsilon_r \leq -2$, respectively. It is also notable that when the origin is inside of the volume, then L_{zz} is always either larger than or equal to L_{xx} and L_{yy}, making the component which is perpendicular to the particle's surface the one more likely to cause problems.

If the assumption that depolarization factors of truncated cubes behave similarly to truncated spheres holds, we see that the volume elements on a surface that is close to perpendicular to the external electric field are those most likely to cause problems. This is because the dipoles on surfaces that are parallel to the electric field E^{out} can only have their singularities at very negative values of ϵ_r. It should also be noted that near the singularity the direction of the polarizability can also vary wildly compared to the ideal case, because the sign of α_i is different on different sides of the singularity.

If we look at the strength of the electric field on the surface of the 10 nm silver sphere at its absorption peak, we can see how the electric field seems to be concentrated on the 'steps' that have been caused by the discretization. This is presented in Fig. 14. The same can be observed, though less clearly, for the 100 nm sphere at its scattering peak, as seen in Fig. 15. We also see that the strongest variation in the electric field on the surface does seem to happen around the poles.

Also, for the infinite cylinders seen in Fig. 8 and the case of the infinite film in Fig. 9, we see that the structures which only have surfaces parallel to the

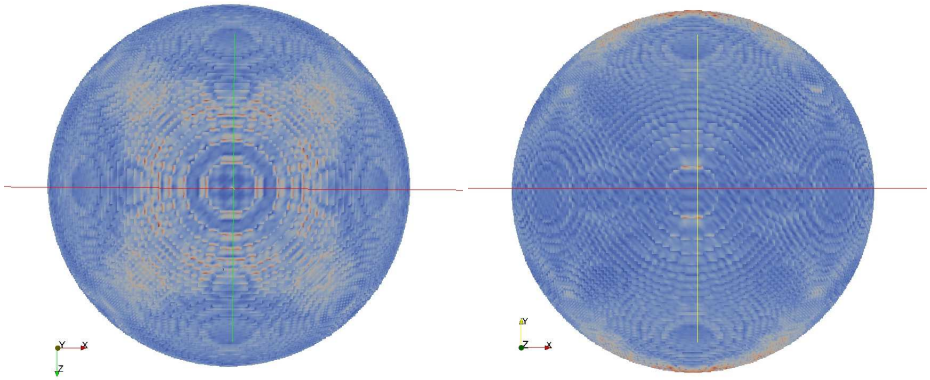

Figure 14: The strength of the electric field on the surface of a 10^6 dipole 10 nm silver sphere at the wavelength of 356.6 nm, i.e., at the absorption peak. The incident electric field is polarized along the y-axis and the wave travels along the x-axis. The field is strongest at the steps which are caused by the cubic discretization.

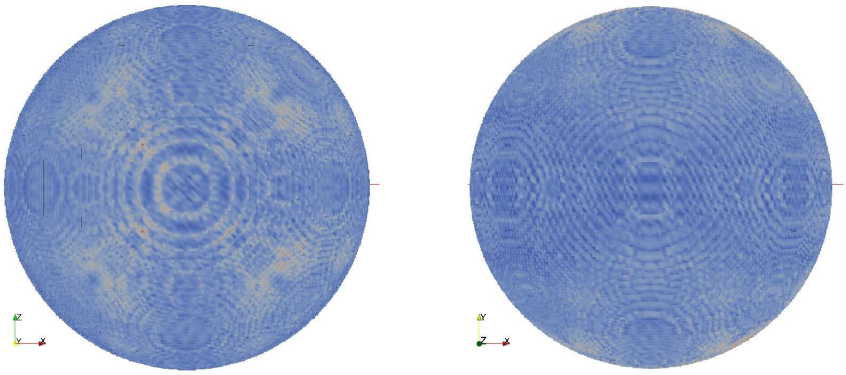

Figure 15: The strength of the electric field on the surface of a 10^6 dipole 100 nm silver sphere at the wavelength of 400.8 nm, i.e., at the computed scattering peak. The incident electric field is polarized along the y-axis and the wave travels along the x-axis. The field is strongest at the steps which are caused by the cubic discretization.

electric field behave well. The major difference between the left and right side of Fig. 8 is that on the right the electric field is partly perpendicular to the surface of the cylinder and this leads to charge density on the surface.

This knowledge may be used in order to predict whether a particular shape is likely to require a very large number of dipoles before good accuracy is achieved. It will not give us exact numbers, but it may still be used as a rule of thumb. The defining factors for the internal field seem to be whether the particle's surfaces are such that they would need to consist of truncated elements, and if so, whether one may expect the electric field to be perpendicular to those surfaces. If such surfaces exist, then slow convergence with dipole count may be expected, especially if the structure is thin, such as in the case of the core shell particles.

Unlike in DDA, when an irregular tetrahedral grid is used, all of the dipoles at the surface are more likely to be about at the same depth from the surface, and so the polarizability at the surface does not vary as much as in the case of a regular cubic grid.

It should also be noted that the polarizability given by Eqs. (9) and (11) is, similarly to the Clausius–Mossotti polarizability, only accurate at the long wavelength limit. Most implementations of DDA that are used in practice include some kind of finite wavelength correction. In practice it may be possible to circumvent the problems with plasmonic particles by using a geometry correction similar to that introduced by Rahmani et al. [44] or Collinge and Draine [45], which were developed to make DDA more accurate at long wavelengths and for high indices of refraction. They also already take the finite sizes of the dipoles into account, although they also require the static-limit solution of the problem to be known, which limits their usefulness. Testing these, however is outside of the scope of this work. Another potential solution is to use the weighted discretization (WD) scheme developed by Piller [46, 47]. This method takes the shape of the particle's surface into account by calculating an effective permittivity for the surface dipoles by using volume fraction weighting and the electromagnetic interface conditions between the particle and its surrounding medium. Again, it is unfortunately outside the scope of this article to test WD in the problem region.

5. Conclusions

The convergence of DDA with increasing dipole count has been tested in a region of slow convergence previously discovered by Yurkin [19, 20], using different particle shapes and silver as the plasmonic material. We have found that the internal electric fields of the particles are strongly dependent on the discretization used, and that they vary in an unphysical way. These results are compared with a boundary element method (BEM).

Our conclusions support the view, that the problems with DDA for plasmonic particles are caused by the improper handling of the surfaces when the complex index of refraction of the material $\tilde{n}$ becomes entirely or almost purely imaginary. For complex permittivity ϵ_r this corresponds to the region where

$\epsilon' < 0$ and $\epsilon'' << 1$. This is similar to results that has been reported by Yurkin et al. [18, 19], and Andersen et al. [43] in relation to infrared absorption of SiO_2 and SiC particles.

Our interpretation is that in DDA the polarizabilities of the volume elements on the surface of the particle are identical to those inside and because of this, they do not have resonances at the same values of ϵ_r, as they would if the shapes of those elements was properly taken into account. In other words, the elements on the surface do not behave resonantly, as they should if their shapes were properly taken into account. This leads to extremely large errors on the surface, as compared to the ideal case where the resonances appear.

It is intuitively easy to understand that when the behavior of an object is dominated by a surface phenomenon, such as the LSPR, it becomes important that the behavior of the surface is properly modeled. Especially the cases of the core-shell particles in Figs. 5 and 6, which have a large part of the silver dipoles located on surfaces, are badly affected by surface errors.

We propose that the physical explanation presented here can be used to predict when problems can be expected with DDA, in the described region of the complex refractive index. Surfaces which cannot be accurately portrayed by cubical dipoles and which can also be expected to be perpendicular to the electric field are an indication of poor performance, especially if the particle also happens to be thin in the same area. It may be possible, that these problems may be entirely avoided in the future if a proper correction for DDA is introduced.

However, we suggest that for now in order to ensure good accuracy with reasonable computation times in the problematic region, a surface integral based method, such as the boundary element method (BEM), may be a better option in the corresponding region of the complex refractive index.

Acknowledgements

This work was funded by Aalto Energy Efficiency Research Programme (EXPECTS-project) and supported in part by the Academy of Finland through its COMP CoE Grant #251748 and by the ERC Advanced Grant No 320773 entitled "Scattering and Absorption of Electromagnetic Waves in Particulate Media" (SAEMPL). The authors wish to acknowledge CSC IT Center for Science, Finland, for computational resources.

References

[1] M. Faraday, The Bakerian lecture: experimental relations of gold (and other metals) to light, Philosophical Transactions of the Royal Society of London 147 (1857) 145–181.

[2] G. Mie, Beiträge zur Optik trüber Medien, speziell kolloidaler Metallösungen, Annalen der Physik 330(3) (1908) 377–445. doi:10.1002/andp.19083300302.

[3] J. Mock, M. Barbic, D. Smith, D. Schultz, S. Schultz, Shape effects in plasmon resonance of individual colloidal silver nanoparticles, Journal of Chemical Physics 116 (2002) 6755–6759. doi:10.1063/1.1462610.

[4] H. Wang, D. Brandl, F. Le, P. Nordlander, N. Halas, Nanorice: A Hybrid Plasmonic Nanostructure, Nano Letters 6 (2006) 827–832. doi:10.1021/nl060209w.

[5] Y. Okuno, K. Nishioka, A. Kiya, N. Nakashima, A. Ishibashi, Y. Niidome, Uniform and controllable preparation of Au-Ag core-shell nanorods using anisotropic silver shell formation on gold nanorods, Nanoscale 2.8 (2010) 1489–1493. doi:10.1039/C0NR00130A.

[6] A. Taflove, Computational Electrodynamics: The Finite-Difference Time-Domain Method, Artech House, Boston, 1995.

[7] P. Ylä-Oijala, M. Taskinen, J. Sarvas, Surface integral equation method for general composite metallic and dielectric structures with junctions, Progress in Electromagnetic Research 52 (2005) 81–108. doi:10.2528/PIER04071301.

[8] E. Purcell, C. Pennypacker, Scattering and Absorption of Light by Nonspherical Dielectric Grains, The Astronomical Journal 186 (1973) 705–714. doi:10.1086/152538.

[9] M. Yurkin, M. Kahnert, Light scattering by a cube: accuracy limits of the discrete dipole approximation and the t-matrix method, Journal of Quantitative Spectroscopy & Radiative Transfer 123 (2013) 176–183. doi:10.1016/j.jqsrt.2012.10.001.

[10] M. Yurkin, V. Maltsev, A. Hoekstra, Convergence of the discrete dipole approximation. I. Theoretical analysis, Journal of Optical Society of America A 23 (2006) 2578–2591. doi:10.1364/JOSAA.23.002578.

[11] M. Mishchenko, V. Tishkovets, L. Travis, B. Cairns, J. Dlugach, L. Liu, V. Rosenbush, N. Kiselev, Electromagnetic scattering by a morphologically complex object: Fundamental concepts and common misconceptions, Journal of Quantitative Spectroscopy & Radiative Transfer 112 (2011) 671–692. doi:10.1016/j.jqsrt.2010.03.016.

[12] M. Yurkin, A. Hoekstra, The discrete dipole approximation: an overview and recent developments, Journal of Quantitative Spectroscopy & Radiative Transfer 106 (2007) 558–589. doi:10.1016/j.jqsrt.2007.01.034.

[13] E. Hao, G. Schatz, Electromagnetic fields around silver nanoparticles and dimers, Journal of Chemical Physics 120 (2004) 357–366. doi:10.1063/1.1629280.

[14] K. Kelly, E. Coronado, L. Zhao, G. Schatz, The Optical Properties of Metal Nanoparticles: The Influence of Size, Shape, and Dielectric Environment, Journal of Physical Chemistry B 107 (2003) 668–677. doi:10.1021/jp026731y.

[15] V. Amendola, O. Bakr, F. Stellacci, A Study of the Surface Plasmon Resonance of Silver Nanoparticles by the Discrete Dipole Approximation Method: Effect of Shape, Size, Structure, and Assembly, Plasmonics 5 (2010) 85–97. doi:10.1007/s11468-009-9120-4.

[16] C. Noguez, Surface Plasmons on Metal Nanoparticles: The Influence of Shape and Physical Environment, Journal of Physical Chemistry C 111 (2007) 3806–3819. doi:10.1021/jp066539m.

[17] I. Sosa, C. Noguez, R. Barrera, Optical Properties of Metal Nanoparticles with Arbitrary Shapes, Journal of Physical Chemistry B 107 (2003) 6269–6275. doi:10.1021/jp0274076.

[18] M. Yurkin, D. de Kanter, A. Hoekstra, Accuracy of the discrete dipole approximation for simulation of optical properties of gold nanoparticles, Journal of Nanophotonics 4 (2010) 41585–41615. doi:10.1117/1.3335329.

[19] M. Yurkin, Computational approaches for plasmonics, in: F. Della Sala, S. D'Agostino (Eds.), Handbook of Molecular Plasmonics, CRC Press, Boca Raton, 2013. doi:10.4032/9789814303217.

[20] M. Yurkin, Challenges in simulation of optical properties of metallic nanoparticles using the discrete dipole approximation, AIP Conference Proceedings 1475 (2012) 98–100. doi:10.1063/1.4750108.

[21] M. Karamehmedović, R. Schuh, V. Schmidt, T. Wriedt, C. Matyssek, W. Hergert, A. Stalmashonak, G. Seifert, O. Stranik, Comparison of numerical methods in near-field computation for metallic nanoparticles, Optics Express 19 (2011) 8939–8953. doi:10.1364/OE.19.008939.

[22] M. Yurkin, A. Hoekstra, The discrete-dipole-approximation code ADDA: Capabilities and known limitations, Journal of Quantitative Spectroscopy & Radiative Transfer 112 (2011) 2234–2247. doi:10.1016/j.jqsrt.2011.01.031.

[23] B. Draine, P. Flatau, Discrete-dipole approximation for scattering calculations, Journal of Optical Society of America A 11 (1994) 1491–1499. doi:10.1364/JOSAA.11.001491.

[24] A. Yaghjian, Electric Dyadic Green's Functions in the Source Region, Proceedings of the IEEE 68 (1980) 248–263. doi:10.1109/PROC.1980.11620.

[25] D. Gutkowicz-Krusin, B. Draine, Propagation of electromagnetic waves on a rectangular lattice of polarizable points, http://arxiv.org/abs/astro-ph/0403082 (2004).

[26] G. Goedecke, S. O'Brien, Scattering by irregular inhomogeneous particles via the digitized Greens function algorithm, Applied Optics 27 (1988) 2431–2438. doi:10.1364/AO.27.002431.

[27] F. D. Sala, S. DAgostino, Handbook of Molecular Plasmonics, Pan Stanford Publishing, Singapore, 2013.

[28] B. Draine, The discrete dipole approximation and its application to interstellar graphite grains, The Astrophysical Journal 333 (1988) 848–872. doi:10.1086/166795.

[29] B. Draine, J. Goodman, Beyond Clausius-Mossoti: Wave propagation on a polarizable point lattice and the discrete dipole approximation, The Astronomical Journal 405 (1993) 685–697. doi:10.1086/172396.

[30] A. Lakhtakia, G. Mulholland, On 2 numerical techniques for light-scattering by dielectric agglomerated structures, Journal of research of the National Institute of Standards and Technology 98 (1993) 699–716.

[31] M. Yurkin, M. Min, A. Hoekstra, Application of the discrete dipole approximation to very large refractive indices: Filtered coupled dipoles revived, Physical Review E 82 (2010) 036703–1–12. doi:10.1103/PhysRevE.82.036703.

[32] M. Yurkin, A. Hoekstra, User Manual for the Discrete Dipole Approximation Code ADDA 1.2, http://a-dda.googlecode.com/svn/tags/rel_1.2/doc/manual.pdf (2013).

[33] S. Rao, D. Wilton, A. Glisson, Electromagnetic scattering by surfaces of arbitrary shape, IEEE Transactions on Antennas and Propagation 30 (1982) 409–418. doi:10.1109/TAP.1982.1142818.

[34] P. Ylä-Oijala, M. Taskinen, Calculation of CFIE impedance matrix elements with RWG and nxRWG functions, IEEE Transactions on Antennas and Propagation 51 (2003) 1837–1846. doi:10.1109/TAP.2003.814745.

[35] S. Järvenpää, M. Taskinen, P. Ylä-Oijala, Singularity subtraction technique for high-order polynomial vector basis functions on planar triangles, IEEE Transactions on Antennas and Propagation 54 (2006) 42–49.

[36] M. Reid, S. Johnson, Efficient computation of power, force, and torque in BEM scattering calculations, http://arxiv.org/abs/1307.2966 (2014).

[37] P. Johnson, R. Christy, Optical Constants of the Noble Metals, Physical Review B 6 (1972) 4370–4379. doi:10.1103/PhysRevB.6.4370.

[38] H. Wallén, H. Kettunen, A. Sihvola, Composite near-field superlens design using mixing formulas and simulations, Metamaterials 3 (2009) 129–139. doi:10.1016/j.metmat.2009.08.002.

[39] B. Draine, P. Flatau, Discrete-dipole approximation for periodic targets: theory and tests, Journal of Optical Society of America A 25 (2008) 2693–2703. doi:10.1364/JOSAA.25.002693.

[40] J. Markkanen, P. Ylä-Oijala, A. Sihvola, Discretization of volume integral equation formulations for extremely anisotropic materials, IEEE Transaction on Antennas and Propagation 60 (2012) 5195–5202. doi:10.1109/TAP.2012.2207675.

[41] J. Markkanen, Discrete Helmholtz Decomposition for Electric Current Volume Integral Equation Formulation, IEEE Trans. Ant. Propag. 62 (2014) 6282–6289. doi:10.1109/TAP.2014.2364614.

[42] L. Gürel, K. Sertel, I. Sendur, On the choice of basis functions to model surface electric current densities in computational electromagnetics, Radio Sci. 34 (1999) 1373–1387. doi:10.1029/1999RS900008.

[43] A. Andersen, H. Mutschke, T. Posch, M. Min, A. Tamanai, Infrared extinction by homogeneous particle aggregates of SiC, FeO and SiO_2 : Comparison of different theoretical approaches, Journal of Quantitative Spectroscopy & Radiative Transfer 100 (2006) 4–15. doi:10.1016/j.jqsrt.2005.11.061.

[44] A. Rahmani, P. Chaumet, G. Bryant, On the importance of local-field corrections for polarizable particles on a finite lattice: Application to the discrete dipole approximation, The Astrophysical Journal 607 (2004) 873–878. doi:10.1086/383609.

[45] M. Collinge, B. Draine, Discrete-dipole approximation with polarizabilities that account for both finite wavelength and target geometry, Journal of Optical Society of America A 21 (2004) 2023–2028. doi:10.1364/JOSAA.21.002023.

[46] N. Piller, Influence of the edge meshes on the accuracy of the coupled-dipole approximation, Opt. Lett. 22 (1997) 1674–1676. doi:10.1364/OL.22.001674.

[47] N. Piller, Coupled-dipole approximation for high permittivity materials, Opt. Commun. 160 (1999) 10–14. doi:10.1016/S0030-4018(98)00645-2.